JOURNAL OF PROPULSION AND POWER
Vol. 20, No. 2, March–April 2004

Compressible Subsonic Particle-Laden Flow over a Square Cylinder

G. B. Jacobs*
University of Illinois at Chicago, Chicago, Illinois 60607
D. A. Kopriva†
Florida State University, Tallahassee, Florida 32306
and
F. Mashayek‡
University of Illinois at Chicago, Chicago, Illinois 60607

Results are presented from simulations of transient vortex shedding in a particle-laden compressible flow over a square cylinder. The carrier phase is computed by solving the Navier–Stokes equations directly with a Chebyshev spectral element method. The dispersed phase is solved by a Lagrangian method, tracking the particles by way of the Basset–Boussinesq–Oseen equation. The coupling between the two phases is one way, that is, the volume fraction of the particles is assumed to be small so the effect of particles on the carrier phase is neglected. The results show that the main effect of the carrier-phase compressibility is the compression of the fluid in front of the cylinder and its expansion behind the cylinder. The particle phase shows the well-known focusing effect for high particle to fluid density ratios. For a lower density ratio, forces such as the pressure drag, virtual mass, Basset history, and Saffman lift tend to increase the dispersion. Compressibility effects are noticeable at low density ratios. In such situations, a lower deposition of the particles at the front of the square and a lower capture of the particles behind the square is observed.

Nomenclature

A_c = particle relative acceleration
C_A = virtual mass correction factor for high Reynolds numbers
C_{Ds} = Stokes drag correction factor for high Reynolds numbers
C_{dp} = pressure drag coefficient
C_H = Basset history correction factor for high Reynolds numbers
C_p = specific heat of the fluid
c_p = pressure coefficient, $(p - p_\infty)/(\rho u_\infty^2/2)$
d_d = particle diameter
e = energy flux
$\boldsymbol{F}$ = flux vector in x direction
Fo = pressure force
f = shedding frequency
$\boldsymbol{G}$ = flux vector in y direction
H = height of the computational domain
L_f = reference length
L_r = reattachment length
M = Mach number, $uM_f/\sqrt{T}$
M_f = reference Mach number, $U_f/\sqrt{\gamma RT_f}$
Pr = Prandtl number, $C_p\mu/\kappa$
p = pressure of the fluid, $\rho T/\gamma M_f^2$
$\boldsymbol{Q}$ = vector of solution unknowns in physical space
R = gas constant
Re_d = particle Reynolds number, $Re_f \rho_{fd} d_d |\boldsymbol{v}_{fd} - \boldsymbol{v}_d|$
Re_f = reference Reynolds number, $\rho_f U_f L_f/\mu$
Sr = Strouhal number, ft_f
St = Stokes number, t_d/t_f
T = temperature
t = time
t_f = flow timescale, L_f/U_f
U_f = reference velocity
u = velocity of the fluid in x direction
v = velocity of the fluid in y direction
v_r = relative particle velocity
W = width of the square cylinder
X_d = downstream length of computational domain
X_u = upstream length of computational domain
x = spatial coordinate in physical space
y = spatial coordinate in physical space
γ = ratio of the specific heats of the fluid
ϵ = particle to fluid density ratio
κ = thermal conductivity
ρ = density
τ = shear stress
ϕ = $t_d f$ ratio of the particle time constant and the time scale of the vortex shedding
Ω = vorticity

Subscripts

d = particle properties
f = reference variable
fd = carrier-phase properties at particle position
t = derivative with respect to t
tot = total carrier-phase property
x = derivative with respect to x
$-x$ = x direction
y = derivative with respect to y
$-y$ = y direction
$-z$ = z direction
1 = x direction of τ or the x-plane τ is acting on
2 = y direction of τ or the y-plane τ is acting on
∞ = freestream conditions

Received 6 February 2003; revision received 4 September 2003; accepted for publication 10 September 2003.

*Graduate Assistant, Department of Mechanical and Industrial Engineering, 842 West Taylor Street. Student Member AIAA.
†Professor, Department of Mathematics.
‡Associate Professor, Department of Mechanical and Industrial Engineering, 842 West Taylor Street; mashayek@uic.edu. Associate Fellow AIAA.

Superscripts

a = advective flux
v = viscous flux
$\bar{}$ = time-averaged quantity
$\tilde{}$ = Favre time-averaged quantity

Introduction

IN this paper, we study numerically the transient particle-laden compressible flow over a square cylinder. This type of flow has relevance to numerous engineering applications, such as flame holders in spray or coal combustors. The unconfined single-phase flow around this configuration has been subject to numerous investigations. However, thus far mostly incompressible flows have been considered. Refer to Ref. 1 for a review of both experimental and numerical studies. The numerical studies have been limited to low-order finite difference and finite volume methods, and to the best of the authors' knowledge, no study of this flow employing a high-order spectral method has been reported.

On the other hand, the particle-laden flow around the square cylinder has not been subject of much investigation. A similar configuration was investigated in Brandon and Aggarwal,[2] but in that study the flow was confined on both sides by walls. Several studies exist on particle dispersion in shear flows whose dynamics are dominated by large-scale vortices similar to those found in the flow around the square cylinder. According to Brandon and Aggarwal,[2] the dispersion behavior is similar to that reported in homogeneous flows, where the particles collect preferentially in regions of low vorticity and high strain rate. In later investigations, for example, Tang et al.,[3] it was shown that the particle dispersion in shear flows whose dynamics are dominated by large-scale vortex dynamics is characterized by the Stokes number. Here, the Stokes number is defined as the ratio of the particle response time to a characteristic flow time. At a Stokes number of unity, it was observed that the particles distribute along the periphery of the vortices, which is now generally known as particle focusing. Burns et al.[4] showed, through a perturbation study, that particle focusing in a plane far wake past a bluff body is the consequence of the presence of a periodic attractor in the phase space of the dynamic system governing the particle motion. Only Brandon and Aggarwal[2] took into account the effects of pressure drag, virtual mass, history force, and Saffman lift force on the dispersed phase through the Basset–Boussinesq–Oseen (BBO) equation. The other studies considered only the Stokes drag on the particle.

In this study, we revisit the particle-laden flow around a rectangular cylinder, but consider the compressible flow and an unconfined configuration. The dispersion behavior for the particle phase is investigated for different Stokes numbers and particle to fluid density ratios. We will focus primarily on the effects of compressibility on the single-phase flow and the dispersion behavior of the solid particles.

The paper is organized as follows. First the governing equations and numerical treatment of both the carrier and the dispersed phases are presented. Next, the results for the carrier phase at different Mach numbers are discussed. Then the results for the dispersion behavior of the particles at different Stokes numbers, density ratios, and carrier-phase freestream Mach numbers are presented, followed by concluding remarks.

Formulation and Methodology

For the carrier phase, we consider a compressible and Newtonian fluid, with no bulk viscosity, that is assumed to obey the perfect gas equation of state. The two-dimensional Navier–Stokes equations for the fluid are given, in dimensionless form, by

$$\boldsymbol{Q}_t + \boldsymbol{F}^a_x + \boldsymbol{G}^a_y = 1/\left[Re_f\left(\boldsymbol{F}^v_x + \boldsymbol{G}^v_y\right)\right] \tag{1}$$

where

$$\boldsymbol{Q} = \begin{bmatrix} \rho \\ \rho u \\ \rho v \\ \rho e \end{bmatrix}, \qquad \boldsymbol{F}^a = \begin{bmatrix} \rho u \\ p + \rho u^2 \\ \rho uv \\ u(\rho e + p) \end{bmatrix}$$

$$\boldsymbol{G}^a = \begin{bmatrix} \rho v \\ \rho uv \\ p + \rho v^2 \\ v(\rho e + p) \end{bmatrix} \tag{2}$$

The energy flux e is defined using the ideal gas relation as $\rho e = p/(\gamma - 1) + \rho(u^2 + v^2)/2$, where $\gamma = 7/5$. The viscous fluxes are expressed as

$$\boldsymbol{F}^v = \begin{bmatrix} 0 \\ \tau_{11} \\ \tau_{21} \\ u\tau_{11} + v\tau_{21} + \dfrac{1}{(\gamma - 1)M_f^2 Pr} T_x \end{bmatrix}$$

$$\boldsymbol{G}^v = \begin{bmatrix} 0 \\ \tau_{12} \\ \tau_{22} \\ u\tau_{12} + v\tau_{22} + \dfrac{1}{(\gamma - 1)M_f^2 Pr} T_y \end{bmatrix} \tag{3}$$

where, under the Stokes hypothesis, the shear stresses are given by

$$\tau_{11} = 2[u_x - (u_x + v_y)/3]$$

$$\tau_{22} = 2[v_y - (u_x + v_y)/3]$$

$$\tau_{12} = v_x + u_y \tag{4}$$

The subscript on the stress tensor τ defines the direction of τ and the plane it is acting on, where 1 and 2 are the x and y directions, respectively. The equation of state is $p = \rho T/\gamma M_f^2$. All of the variables are normalized by reference length L_f, density ρ_f, velocity U_f, and temperature T_f scales. The reference Reynolds and Mach numbers are defined by $Re_f = \rho_f U_f L_f/\mu$ and $M_f = U_f/(\gamma R T_f)^{1/2}$, respectively, and the Prandtl number is $Pr = C_p\mu/\kappa$.

The particles are assumed to remain spherical and do not evaporate. A one-way coupling between the carrier phase and the particle phase is assumed, that is, the effect of the particles on the carrier phase is neglected. They are tracked individually in a Lagrangian manner, with the instantaneous particle position and velocity given by $\boldsymbol{x}_d$ and $\boldsymbol{v}_d$. The Lagrangian equations for particle position and velocity, nondimensionalized with U_f and L_f, are given by[5]

$$\frac{\mathrm{d}\boldsymbol{x}_d}{\mathrm{d}t} = \boldsymbol{v}_d \tag{5}$$

$$\frac{\mathrm{d}\boldsymbol{v}_d}{\mathrm{d}t} = \frac{C_{Ds}}{St}(\boldsymbol{v}_{fd} - \boldsymbol{v}_d) + C_A \frac{1}{\epsilon}\frac{\mathrm{d}}{\mathrm{d}t}(\boldsymbol{v}_{fd} - \boldsymbol{v}_d) + \frac{1}{\epsilon}\frac{\mathrm{D}(\boldsymbol{v}_{fd})}{\mathrm{D}t}$$
$$+ \frac{0.2C_H}{(\epsilon \mathrm{St})^{\frac{1}{2}}} \int_{t_0}^{t} \frac{\mathrm{d}(\boldsymbol{v}_{fd} - \boldsymbol{v}_d)/\mathrm{d}\tau}{\sqrt{t - \tau}} \mathrm{d}\tau + \frac{0.727}{(\epsilon \mathrm{St}|\boldsymbol{\Omega}|)^{\frac{1}{2}}}$$
$$\times \begin{bmatrix} (v_{fd-y} - v_{d-y})\Omega_{-z} \\ -(v_{fd-x} - v_{d-x})\Omega_{-z} \end{bmatrix} \tag{6}$$

where

$$\frac{\mathrm{D}}{\mathrm{D}t} = \frac{\partial}{\partial t} + v_{fd-x}\frac{\partial}{\partial x} + v_{fd-y}\frac{\partial}{\partial y} \tag{7}$$

$$\frac{\mathrm{d}}{\mathrm{d}t} = \frac{\partial}{\partial t} + v_{d-x}\frac{\partial}{\partial x} + v_{d-y}\frac{\partial}{\partial y} \tag{8}$$

Equation (6) is the so-called BBO equation. The terms on the right-hand side represent, in order, the effects of the steady state drag, the virtual mass force, the pressure drag, the Basset history force, and the Saffman lift force.

In Eq. (6), $\boldsymbol{\Omega} = \nabla \times \boldsymbol{v}_{fd}$ is the vorticity of the carrier phase and $\epsilon = \rho_d/\rho_{fd}$ is the ratio of the particle to fluid density. The Stokes number is defined as

$$\mathrm{St} = \frac{t_d}{t_f} = \frac{d_d^2 \rho_d Re_f}{18} \tag{9}$$

where t_d is the particle response time and t_f is a characteristic flow time, defined here as the ratio of the square width to the inflow velocity.

The preceding equations were derived for $Re_d < 1$. Correction factors for high particle Reynolds numbers have been developed and are given as

$$C_{Ds} = 1 + \left(Re_d^{\frac{2}{3}}/6\right) \tag{10}$$

for the Stokes drag,[5]

$$C_A = 1.05 - \left[0.066/\left(A_c^2 + 0.12\right)\right] \tag{11}$$

for the virtual mass force,[6] and

$$C_H = 2.88 + \left[3.12/(1 + A_c)^3\right] \tag{12}$$

for the Basset history force (see Ref. 6). Here, A_c represents the relative acceleration factor defined as

$$A_c = \frac{v_r^2}{d_d} \Big/ \frac{\mathrm{d}v_r}{\mathrm{d}t} \tag{13}$$

where v_r is the relative particle velocity.

The carrier phase is solved with a multidomain Chebyshev spectral method. The method has been described and tested extensively in previous papers[7–10] and so for brevity will not be explained here. To track the particles a tracking algorithm has been developed as described in detail in Ref. 9. The algorithm uses a second order Adams–Bashforth scheme for time integration of the particle equations. A sixth-order Lagrangian scheme interpolates the carrier-phase variables to the particle position.

Results and Discussion of Carrier-Phase Flow

The single-phase flow around a square cylinder was investigated in our previous work on testing boundary conditions.[10] The flow was computed for freestream Reynolds and Mach numbers of $Re_f = 200$ and $M_\infty = 0.1$, which ensured a transitional vortex shedding and nearly incompressible flow. The study showed that choosing the dimensions of the computational domain, defined in Fig. 1a, to be $X_u = 8.5$, $X_d = 30$, and $H = 17$ gives. Figure 1b shows the grid that led to a grid-independent solutions for which boundary effects are

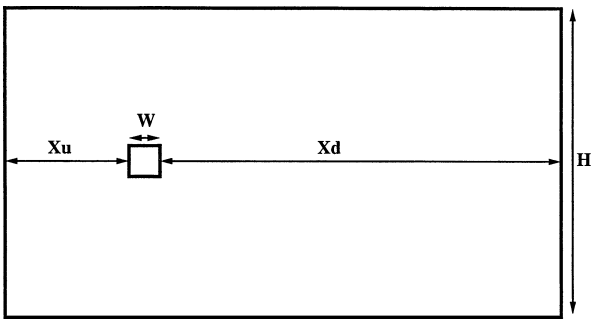

Fig. 1a Computational domain.

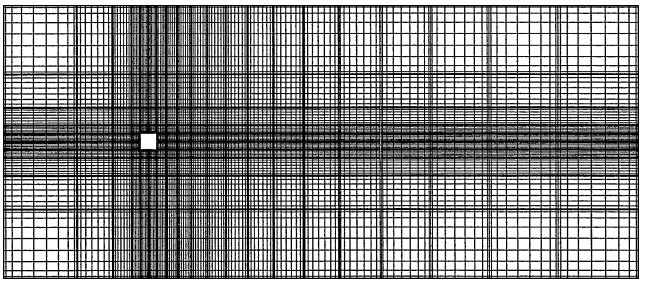

Fig. 1b Grid around square cylinder.

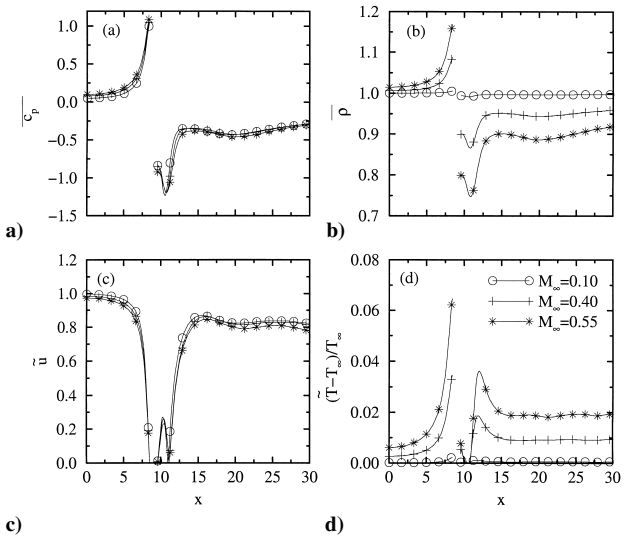

Fig. 2 Time-average parameters vs distance x along the centerline for three different freestream Mach numbers M_∞: a) time-averaged pressure coefficient $\overline{c_p}$, b) time-averaged density $\bar{\rho}$, c) Favre time-averaged velocity $\tilde{u}$, and d) Favre time-averaged normalized temperature $(\tilde{T}-T_\infty)/T_\infty$.

insignificant, i.e. unconfined flow. A polynomial of order seven per element was shown to be sufficient. Increasing the polynomial order further to 14 showed less than 1% difference in the averaged flowfield. The boundary conditions were chosen as follows: At the top and right boundaries, a specified pressure boundary condition with characteristic extrapolation on the remaining variables was employed. At the left and bottom, the mean flow values were specified and a Riemann solver was used to match the boundary values with the interior values. Finally, an adiabatic wall was specified for the square cylinder wall with no-slip conditions for the velocity. The need for asymmetric boundary condition treatment at boundaries "far away" from the square is related to the upwinding requirements to satisfy stability of the scheme.[10]

To study the effect of Mach number on the carrier-phase flow, the flow around the square cylinder is computed here for three different freestream Mach numbers $M_\infty = 0.1$, 0.4, and 0.55. The Mach numbers are chosen such that no discontinuities such as shock waves occur. The maximum local Mach number of $M = 0.91$, found in the case with $M_\infty = 0.55$, confirms that shock waves are not likely to occur.

This study concentrates on the time-averaged flow in three regions around the square, each with distinct flow characteristics: The stagnation flow in front of the square, the separated flow on the side of the square, and the shed vortex wake behind the square.

Forward Stagnation Flow

Figure 2 shows four time-averaged flow variables along the centerline. As expected, toward the stagnation point at $x = 8.5$, the Favre averaged velocity magnitude $\tilde{u}$ vanishes. The flow is nearly isentropic, that is, the time-averaged total pressure $\bar{p}_{\mathrm{tot}}$, the time-averaged total density $\bar{\rho}_{\mathrm{tot}}$ and Favre time-averaged temperature $\tilde{T}_{\mathrm{tot}}$

defined as

$$\bar{p}_{\text{tot}} = \bar{p}\{1 + [(\gamma - 1)/2]\bar{M}^2\}^{\gamma/(\gamma-1)}$$

$$\bar{\rho}_{\text{tot}} = \bar{\rho}\{1 + [(\gamma - 1)/2]\bar{M}^2\}^{1/(\gamma-1)}$$

$$\tilde{T}_{\text{tot}} = \tilde{T}\{1 + [(\gamma - 1)/2]\bar{M}^2\} \tag{14}$$

do not change more than 1% toward the stagnation point. Consequently, the forward stagnation pressure, density, and temperature attain their upstream total values. Increasing M_∞ leads to increased total values, thus, explaining the increased time-averaged pressure $\bar{p}$, density $\bar{\rho}$, and normalized temperature $(\tilde{T} - T_\infty)/T_\infty$ with increased M_∞. As a measure for the compressibility effect, the density deviation from the incompressible density value of 1.0 is considered. For $M_\infty = 0.1, 0.4$, and 0.55, this deviation at the forward stagnation point is 0.5, 8.7, and 16.9%, respectively, which compares well to the total density increase of 0.5, 8.2, and 15.8%, respectively.

Separated Side Flow

The sharp forward corner of the square causes the flow to separate. This separation leads to a recirculation vortex on the side wall as shown in Fig. 3a. In the averaged flowfield, it is observed that the side vortex is fed by the recirculation vortex at the rear of the cylinder.

An instantaneous streamline snapshot of flow (Fig. 4) shows that the strong rearward vortex feeds the side vortex at the time when it is about to shed off: The side vortex is then lifted off the side wall, and the rearward vortex gives some of its vorticity to the side vortex. This phenomenon is observed for all M_∞ values studied. Furthermore, the location of the separation streamline on the side does not change significantly with M_∞.

Outside the separating streamline (or side vortex), the flow accelerates from front to rear because the increased potential energy at the stagnation point is converted to kinetic energy at the side. For increasing M_∞, the Favre averaged velocity does not change significantly at this location due to the invariance of the separating streamline. Other variables, $\tilde{T}$, $\bar{\rho}$, and $\bar{c_p}$, however, decrease due to the adiabatic expansion of the flow.

Inside the separating streamline (or side vortex) the total flow pressure, temperature, and density decrease as a result of viscous energy dissipation in the shear layer emanating from the front corner because the viscous dissipation decreases the total energy available in a fluid element. As opposed to the decreased total temperature, the normalized static temperature increases as a result of viscous dissipation. At the front corner, a strong suction is present due to the sudden separation of the flow, yielding a sharp drop in $\overline{c_p}$. Increasing M_∞ decreases the density and the normalized static temperature at this point by expansion of the fluid element. Farther downstream along the side of the square, the density increases; however, for higher M_∞, $\bar{\rho}$ remains lower. The increased $\bar{\rho}$ in combination with viscous dissipation in the shear layer leads to a normalized static temperature increase farther downstream along the side. Increasing M_∞ increases the normalized static temperature because of an increased flow compression.

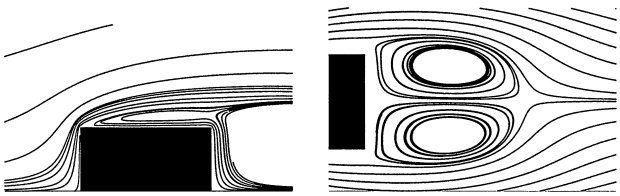

a) b)

Fig. 3 Time-averaged streamlines a) on the side of and b) behind the square cylinder.

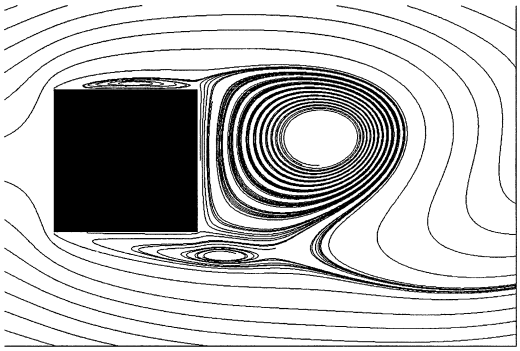

Fig. 4 Snapshot of the streamline pattern around square cylinder.

Vortex-Shedding Behind the Square

The effect of compressibility on four averaged flow variables along the centerline is presented in Fig. 2. Increasing M_∞ decreases $\overline{c_p}$ and $\bar{\rho}$ behind the square due to expansion of the fluid (Figs. 2a and 2b). As a measure for the compressibility effect, the density deviation from the incompressible density value of 1.0 is considered. For $M_\infty = 0.1$, 0.4, and 0.55, this deviation at the back of the square is -0.6, -10.0, and -20.2%, respectively. In contrast to the density and pressure trends, the normalized temperature shows an increase behind the cylinder with increasing M_∞ (Fig. 2d). As already explained, this is due to the convection of heat that is generated on the side to the back of the square. The temperature at the back of the square is lower than the temperature in the front at the stagnation point due to the well-known Eckert–Weise effect (see Ref. 11), which causes the total time-averaged temperature to decrease in the wake as a consequence of energy separation in the vortex street. The energy separation is visualized in Fig. 5a through cold and hot spots in the total temperature field that reside above and below the downstream convected vortices. Time averaging this field leads to the cold wake, as shown by the time-averaged total temperature contours in Fig. 5b. The lower total temperature leads to a lower static temperature because the velocity is zero at the back of the square. The Eckert–Weise effect is stronger for larger M_∞, as can be seen from the larger decrease in temperature for larger M_∞. This does not, however, lead to a decrease of the temperature behind the cylinder, because the total freestream temperature is larger for larger M_∞.

In the transient flow, vortex shedding takes place behind the square. Time averaging the flow shows two recirculation vortices,

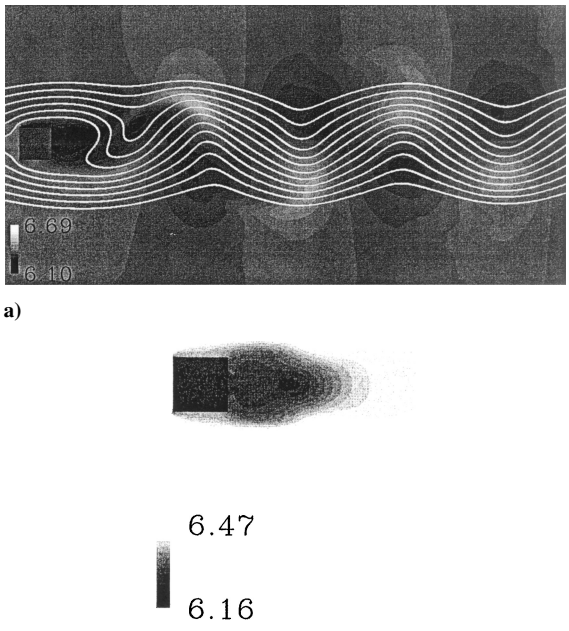

a)

b)

Fig. 5 $M_\infty = 0.40$: a) snapshot of total temperature contours and b) time-averaged total temperature contours.

Table 1 Comparison of various flow parameters for different Mach numbers and $Re_f = 200$

M_∞	L_r	$\tilde{u}_{\max}$	$\overline{C_{dp}}$	Sr
0.10	1.44	0.27	1.49	0.153
0.40	1.60	0.26	1.59	0.147
0.55	1.63	0.23	1.73	0.147

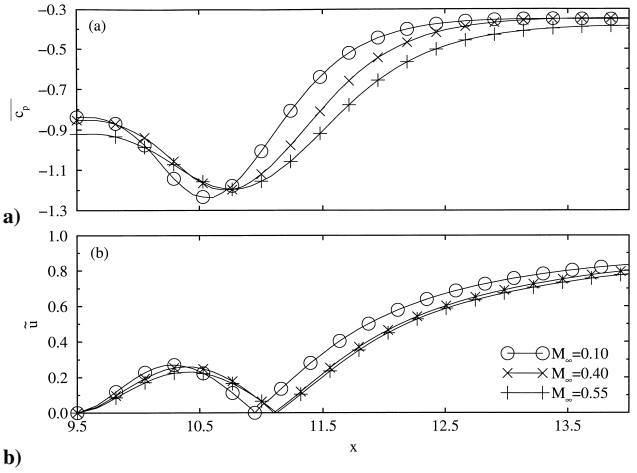

Fig. 6 Three different freestream Mach numbers M_∞: a) time-averaged pressure coefficient $\overline{c_p}$ and b) Favre time-averaged velocity $\tilde{u}$ vs the distance x along the centerline.

as seen in Fig. 3b. In the averaged flowfield, a parameter that typically characterizes the flow, is the reattachment length of these two recirculating vortices L_r. The location of reattachment is the x position, where the Favre time-averaged velocity $\tilde{u} = 0$ along the centerline behind the cylinder. From Figs. 6a and 6b, where $\overline{c_p}$ and $\tilde{u}$ are shown close to the square, we see that increasing M_∞ from 0.1 to 0.4 causes L_r to increase. The values of L_r are given in Table 1. Increasing M_∞ further to 0.55 does not significantly affect L_r. The increase of L_r is a consequence of the expansion of the recirculation vortex. An explanation might be derived from Ref. 12, where it is shown that a decaying free compressible viscous vortex is always compressed because a decrease in kinetic energy of the vortex always leads to positive pressure work term, thus, compressing the vortex. In our case, the vortex increases its kinetic energy before it sheds off, which leads to negative pressure work and, thus, expansion. The reason L_r does not expand further after $M_\infty = 0.4$ is not clear to us. Aside from the reattachment length, the pressure and velocity field show similar trends near the square for all M_∞; however, the values of $\overline{c_p}$ differ. At the square wall, $\overline{c_p}$ is smaller for higher M_∞. The minimum value of $\overline{c_p}$, located just before the reattachment point, increases with increasing M_∞. Farther downstream, $\overline{c_p}$ again is smaller for larger M_∞. The velocity $\tilde{u}$ shows a decreased value for increased M_∞ close to the square. Table 1 shows the maximum velocity $\tilde{u}_{\max}$ within the recirculation vortices as a measure of this effect.

Next, we consider the effect of increased Mach number on the Strouhal number Sr and the time-averaged pressure drag coefficient $\overline{C_{dp}}$. Here, the Strouhal number is defined as

$$Sr = f t_f \tag{15}$$

where f is the frequency of the periodic shedding from the cylinder. The time-averaged pressure drag coefficient is defined as

$$\overline{C_{dp}} = \overline{F_0} \Big/ \left(\rho_f U_f^2 / 2\right) \tag{16}$$

where $\overline{F_0}$ is the time averaged pressure force on the cylinder in the streamwise direction and ρ_f is a reference density, set equal to the inlet density.

Table 1 shows that increasing M_∞ increases $\overline{C_{dp}}$ significantly. As already explained, this is due to the increased compression in front of the cylinder and decreased compression behind it. Increasing M_∞ from 0.1 to 0.4 decreases Strouchal number Sr. Increasing Ma_∞ further to 0.55 has no effect on Strouchal number Sr. The decrease in Strouhal number seems to be related to the increase in L_r. A reason could be that the pressure work that is needed for the expansion of the vortex decreases the vortex strength. The vortex strength needed for the vortex shedding requires a longer time to develop, thus effectively decreasing the Strouhal number.

Results and Discussion of the Dispersed Phase

In this section, we study the dispersion characteristics of the particles in the wake of the square cylinder for various Stokes numbers St, density ratios ϵ, and Mach numbers M_∞. In all cases, 11 particles are released every 0.5 time units at two nondimensional length units in front of the cylinder with a uniform distribution spread over 2 length units in the crossflow direction. Another set of 11 particles are released right behind the cylinder, with the same time interval, and uniformly distributed over the height of the cylinder. The initial particle velocity is equal to the fluid velocity at the particle position.

For the parameter values used here, the continuum fluid assumption for the flow around the particle is narrowly satisfied for the smallest particles. Also, strictly speaking, the largest particles (at $\epsilon = 5$) considered are not small enough to satisfy a one-way coupling. These restrictions can be easily relaxed by increasing the flow Reynolds number, which will be considered in our future studies. Nevertheless, we note that dispersion depends primarily on the Stokes number and the vorticity distribution of the carrier phase. Moreover, it is known that the vortex shedding structures of low Reynolds number transient flows are also found in high Reynolds number flows, thus, expectedly leading to similar dispersion characteristics.

The results for St = 0.05, 1.0, and 5.0 are shown in Figs. 5–7c for $M_\infty = 0.1$ and $\epsilon = 1000$. Figures 7 suggest that, in general, the dispersion behavior is similar to that reported in previous works.[3] Figure 7a shows that the particles follow the flow closely at St = 0.05. This confirms that for St < 0.1 the particles behave like fluid particles. In Fig. 7b, the particles display a preferential distribution around the periphery of the vortices, which, in previous,[3] has been noted as the intermediate Stokes number St behavior. For St = 5.0, Fig. 7c shows that the particles initially follow the fluid much less as compared to the other cases because their response time to the fluid is much higher. Farther downstream, the particles shed in packages similarly to the vortices shed off the cylinder. These packages then reside above or below two counter-rotating vortices, depending on the vertical velocity between the two vortices. The packages originate from the particles that are released behind the cylinder. For all Stokes number St values, this group of particles oscillates up and down behind the square, and the particles accumulate at the top or bottom corner of the square, depending on whether a vortex with positive or negative vorticity is created behind the square. Once the vortex is about to shed off, these accumulated particles surf downstream with the vortex. In the case of St = 5, distinct packages are created because the ratio of the particle time constant and the timescale of the vortex shedding given as

$$\phi = t_d/(1/f) = \mathrm{St}/(1/Sr) \tag{17}$$

is 0.765 for this Stokes number. This value of ϕ is close to unity which indicates that the timescales of the carrier and dispersed phases are close and the accumulation and shedding of the particles closely follows the vortex shedding of the carrier phase, thus, leading to packages. For lower Stokes number, ϕ is significantly smaller than one, and no packages are observed.

Next, we investigate the effect of the particle to fluid density ratio ϵ on the particle distribution. Decreasing the density ratio to $\epsilon = 5$, while keeping Stokes number constant, causes other forces on the particle, such as pressure drag, added mass, and Saffman lift force in Eq. (6), to have a significant influence on the particle

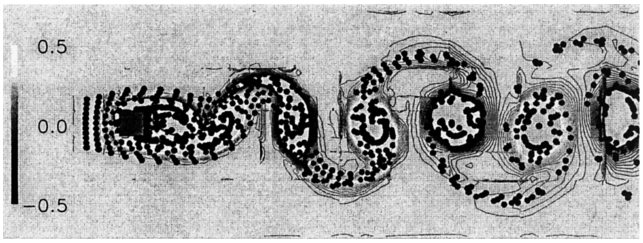

a) St = 0.05

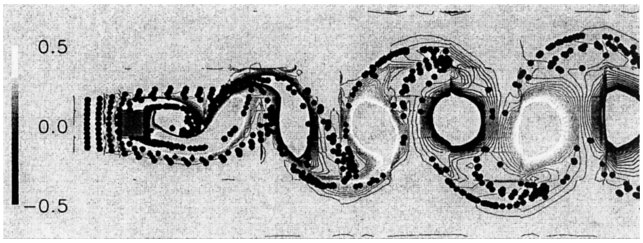

b) St = 1.0

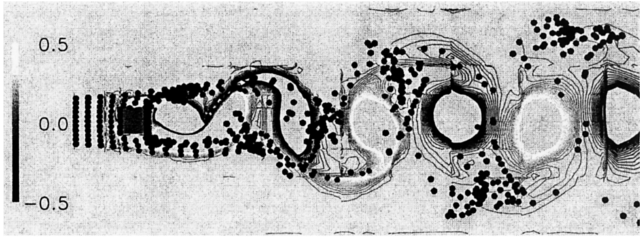

c) St = 5.0

Fig. 7 Snapshots of particles for St = 0.05, 1.0, and 5.0 in transient flow around square cylinder for particle to fluid density ratio $\epsilon = 1000$ and freestream Mach number $M_\infty = 0.1$: ——, instantaneous vorticity of the carrier phase.

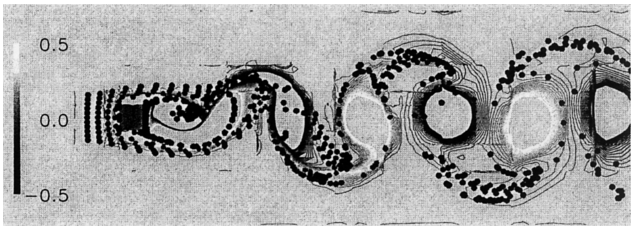

a) St = 1.0

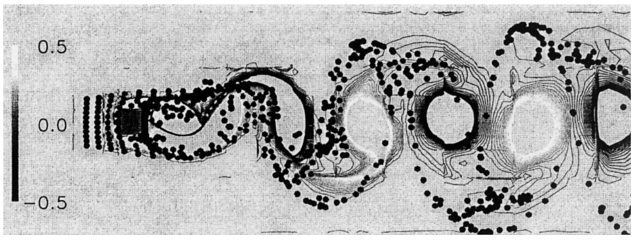

b) St = 5.0

Fig. 8 Snapshots of particles for St = 1.0 and 5.0 in transient flow around square cylinder for particle to fluid density ratio $\epsilon = 5$ and freestream Mach number $M_\infty = 0.1$: ——, instantaneous vorticity.

distribution. In Fig. 8, the results are shown for $\epsilon = 5$ at St = 1.0 and 5.0 with $M_\infty = 0.1$. The effect of ϵ when St = 0.05 was not considered because, as already mentioned, for this Stokes number the particles behave like fluid particles and, thus, will not be affected by the extra forces. When Figs. 7 and 8 are compared, the following is concluded: For a lowered ϵ, the particles are captured more in the near wake, that is, the flow region behind the cylinder. This is because the extra terms are dependent on the velocity gradient

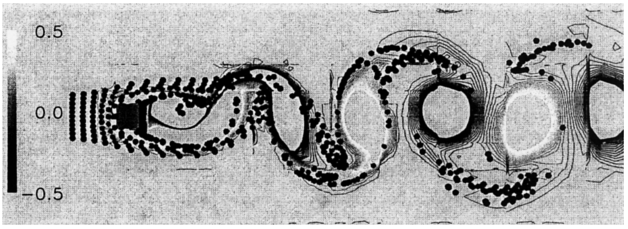

a) St = 1.0

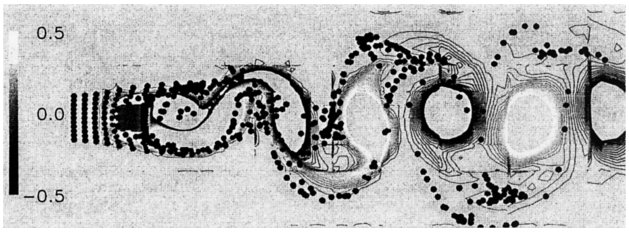

b) St = 5.0

Fig. 9 Snapshots of particles for St = 1.0 and 5.0 in transient flow around square cylinder for particle to fluid density ratio $\epsilon = 5$, and freestream Mach number $M_\infty = 0.55$: ——, instantaneous vorticity.

of the carrier phase, and the shear layer emanating from the square yields high-velocity gradients. Furthermore, the particle distribution becomes more dispersed in the far wake for both Stokes numbers, which is again a consequence of the increased dependency of the extra forces on the velocity gradients in the fluid. These density ratio effects are more noticeable for higher Stokes number because for an increased Stokes number the Stokes drag decreases relatively to the other ϵ-dependent force contributions. The Stokes drag shows this decrease because it has the highest Stokes number dependency in Eq. (6).

Finally, we consider the effect of increased freestream Mach number on the particle distribution. For a high-density ratio, the dispersion characteristics show the same dependency on the Stokes number as for lower M_∞ because at high ϵ the Stokes drag, which is dictated by the velocity field, is the only significant force on the particle. Thus, for high M_∞ and high ϵ, the dispersion will follow the variations in the velocity field, where the main differences are the fluid compression and expansion found directly in front and behind the cylinder. For $\epsilon = 5$, forces other than the Stokes drag in Eq. (6) will be affected by compressibility, mostly through their dependence on the carrier-phase density. Figure 9 shows the results for $\epsilon = 5$ and $M_\infty = 0.55$. When Figs. 8 and 9 are compared, the increased carrier-phase density in front of the cylinder for the higher Mach number causes fewer particles to deposit on the front of the cylinder. Indeed, the higher density causes ϵ to decrease, which in turn yields higher source terms in the particle equation. The higher source terms lead to a higher acceleration of the particles in the cross stream direction so that they do not deposit. A similar mechanism causes the particles to be less captured on the side and the back of the square because the density of the carrier phase decreases in these areas as the Mach number increases. The distribution of the particles in the far wake is similar to the cases where only the Stokes drag is taken into account. These compressibility effects, however, are marginal because the carrier-phase density changes are not very large. The result is a small variation in ϵ and correspondingly small effect on the dispersion characteristics.

Conclusions

We have studied the effects of compressibility on the particle-laden flow around a square cylinder using a staggered-grid spectral method to simulate the carrier phase and a Lagrangian tracking method for the dispersed phase. The influence of the particles on the carrier phase is not accounted for, that is, a one-way coupled flow is assumed. The effect of compressibility on the carrier phase manifests itself by a compressed stagnation area in front of the cylinder in the form of increased time-averaged pressure and density and Favre

averaged temperature. Behind the square, the recirculation vortex experiences an expansion, where the density and pressure are lowered. The carrier-phase temperature increases with the increase of the freestream Mach number M_∞, both in front of and behind the square. In the front, this is due to an increased total temperature. Behind the square, this is due to heat transfer from the sides to the back of the square. Behind the square, however, the temperature increase is not as significant, due to the Eckert–Weise effect that decreases the total temperature. The variation in the pressure field leads to an increased pressure drag coefficient on the cylinder as the freestream Mach number is increased. Increasing the freestream Mach number from 0.1 to 0.4 leads to a 4% decrease of the Strouhal number and a 30% increase of the reattachment length of the recirculation vortices. A further increase to $M_\infty = 0.55$ has no effect on the Strouhal number and the reattachment length.

In the dispersed phase, for intermediate Stokes numbers, the well-known focusing of particles is confirmed. For higher Stokes numbers, the particles shed in packages with a frequency that is similar to the shedding frequency of the carrier phase. For low-density ratios, the effect of forces other than the Stokes drag become important. They cause the particles to be more captured in the near wake and more dispersed in the far wake. Finally, the effect of compressibility is noticeable mostly in the near wake, where an increased fluid density causes the particles to be accelerated more in the cross stream direction. The acceleration changes by no more than 3%, and the effect is, therefore, marginal.

Acknowledgments

The support for this work was provided by the U.S. Office of Naval Research and by the National Science Foundation. The computational resources were provided by the San Diego Supercomputing Center.

References

[1]Sohankar, A., Norberg, C., and Davidson, L., "Low-Reynolds-Number Flow around a Square Rectangular Cylinder at Incidence: Study of Blockage, Onset of Vortex Shedding and Outlet Boundary Condition," *International Journal for Numerical Methods in Fluids*, Vol. 26, No. 1, 1998, pp. 39–56.

[2]Brandon, D. J., and Aggarwal, S. K., "A Numerical Investigation of Particle Deposition on a Square Cylinder Placed in a Channel Flow," *Aerosol Science and Technology*, Vol. 34, No. 4, 2001, pp. 340–352.

[3]Tang, L., Wen, F., Yang, Y., Crowe, C. T., Chung, J. N., and Troutt, T. R., "Self-Organizing Particle Mechanism in a Plane Wake," *Physics of Fluids A*, Vol. 4, No. 10, 1992, pp. 2244–2251.

[4]Burns, T. J., Davis, R. W., and Moore, E. F., "A Pertubation Study of Particle Dynamics in a Plane Wake Flow," *Journal of Fluid Mechanics*, Vol. 384, 1999, pp. 1–26.

[5]Crowe, C., Sommerfeld, M., and Tsuji, Y., *Multiphase Flows with Droplets and Particles*. CRC Press, Boca Raton, FL, 1998.

[6]Odar, F., and Hamilton, W. S., "Forces on a Sphere Accelerating in a Viscous Fluid," *Journal of Fluid Mechanics*, Vol. 18, 1964, pp. 302–314.

[7]Kopriva, D. A., and Kolias, J. H., "A Conservative Staggerd-Grid Chebyshev Multidomain Method for Compressible Flows," *Journal of Computational Physics*, Vol. 125, No. 1, 1996, pp. 244–261.

[8]Kopriva, D. A., "A Staggered-Grid Multidomain Spectral Method for the Compressible Navier–Stokes Equations," *Journal of Computational Physics*, Vol. 244, No. 1, 1998, pp. 142–158.

[9]Jacobs, G. B., Kopriva, D. A., and Mashayek, F., "A Particle Tracking Algorithm for the Multidomain Staggered-Grid Spectral Method," AIAA Paper 2001-0630, 2001.

[10]Jacobs, G. B., Kopriva, D. A., and Mashayek, F., "A Comparison of Outflow Boundary Conditions for the Multidomain Staggered-Grid Spectral Method," *Numerical Heat Transfer, Part B-Fundamentals*, Vol. 44, No. 3, 2003, pp. 225–251.

[11]Kurosaka, M., Gertz, J. B., Graham, J. E., Goodman, J. R., Sundaram, P., Riner, W. C., Kuroda, H., and Hankey, W. L., "Energy Separation in a Vortex Sheet," *Journal of Fluid Mechanics*, Vol. 178, 1987, pp. 1–29.

[12]Colonius, T., Lele, S., and Moin, P., "The Free Compressible Viscous Vortex," *Journal of Fluid Mechanics*, Vol. 230, 1991, pp. 45–73.